This manuscript has been submitted for publication in *Journal of Advances in Modeling Earth Systems*. Please note that, the manuscript is currently under review and has yet to be formally accepted for publication. Subsequent versions of this manuscript may have slightly different content. If accepted, the final version of this manuscript will be available via the 'Peer-reviewed Publication DOI' link.

Wavelet-based wavenumber spectral estimate of eddy kinetic energy: Theory

Takaya Uchida, CNRS takaya.uchida@univ-grenoble-alpes.fr)
Quentin Jamet, INRIA (quentin.jamet@inria.fr)
Andrew C. Poje, CUNY (andrewpoje@gmail.com)
Nico Wienders, FSU (wienders@fsu.edu)
William K. Dewar, FSU (wdewar@fsu.edu)
Bruno Deremble, CNRS (bruno.deremble@univ-grenoble-alpes.fr)

Wavelet-based wavenumber spectral estimate of eddy kinetic energy: Theory

Takaya Uchida[1*], Quentin Jamet[1,2], Andrew C. Poje[3], Nico Wienders[4], William K. Dewar[1,4] & Bruno Deremble[1]

[1]Université Grenoble Alpes, CNRS, IRD, Grenoble-INP, Institut des Géosciences de l'Environnement, France

[2]INRIA, ODYSSEY group, Ifremer, Plouzané, France

[3]Department of Mathematics, College of Staten Island, CUNY, USA

[4]Department of Earth, Ocean and Atmospheric Science, Florida State University, USA

Key Points:

- A wavelet-based spectral method to estimate eddy variability is described.
- Wavenumber spectra of eddies are estimated for a doubly-periodic quasi-geostrophic flow.
- The wavelet and Fourier approach agree well in their estimates of spectra and spectral flux.

*Will be moving to the Center for Ocean-Atmospheric Prediction Studies (COAPS), Florida State University, USA.

Corresponding author: William K. Dewar, `wdewar@fsu.edu`

Abstract

A wavelet-based method is introduced in an oceanographic context to estimate wavenumber spectrum and spectral flux of kinetic energy and enstrophy. We apply this to a numerical simulation of idealized, doubly-periodic quasi-geostrophic flows, i.e. the flow is constrained by the Coriolis force and vertical stratification. The double periodicity allows for a straightforward Fourier analysis. Our wavelet spectra and spectral flux agree well with the canonical Fourier approach but with the additional strengths of negating the necessity for the data to be periodic and being able to extract local anisotropies in the flow.

Plain language summary

Chaotic flows such as the ocean currents, atmospheric winds and turbulence in general are fundamentally impossible to analytically predict, namely, to formulate a mathematical general solution. Nevertheless, the interest in describing such chaotic flows can be found in as old as Leonardo da Vinci's sketch of turbulence. While we cannot obtain an analytical description of turbulence, we can extract statistical information from them and a common descriptor has been the wavenumber spectrum. Spectrum reveals at each spatial scale, the level of variability the flow carries. Here, we re-introduce an alternative method in estimating the spectrum based on wavelet functions.

1 Introduction

Fundamental to the goal of properly modelling climate system dynamics is understanding and quantifying how energy is both distributed, and ultimately transferred, across an extremely broad range of dynamically active space and time scales. In the ocean context, the most common means of quantifying the scale-dependent energy content of a chaotic, turbulent flow field is the energy spectrum (e.g. Taylor, 1938; Kolmogorov, 1941; Charney, 1971; Nastrom & Gage, 1983; Yaglom, 2004) given by the Fourier transform of two-point (spatial or temporal) velocity correlations.

We will focus in this paper on spatial correlations since the behavior of wavenumber spectra are described by 'inertial range' theories predicting spectral slopes and cascades (Vallis, 2006). The standard Fourier approach has had great success in providing us with spectral estimates of energy partition and its straightforward mathematical formulation facilitates the spectral interpretation in the original context, namely statistically homogeneous flows where Fourier decompositions are natural. Issues persist, however, in geophysical flows which are statistically inhomogeneous, anisotropic and non-stationary (Uchida, Jamet, et al., 2021). The assumption of homogeneity lies on the fact that a Fourier transform is a global operator over the entire space-time domain of interest. In other words, the Fourier description of the field conflates different regimes of an inhomogeneous flow. A notable example is in the separated Gulf Stream region where the energetics have been argued to be distinct from the gyre interior (Jamet et al., 2021).

Here, we re-introduce a wavelet-based technique which yields localized psuedo-Fourier one-dimensional wavenumber spectra (Perrier et al., 1995). Wavelets emerged in the 1980s as a way to analyze time and space series in more local manner than was possible using Fourier techniques, although strong parallels and connections are to be found between the two methods (Torrence & Compo, 1998). We will argue the localized nature of wavelets allows us to capture the inhomogeneity and anisotropy in the flow. We then apply the wavelet approach to estimate the horizontal kinetic energy (KE) spectral flux from a doubly-periodic quasi-geostrophic (QG) flow, and to a flow subdomain where periodicity no longer applies. The comparisons illustrate some of the advantages of the wavelet approach.

The paper is organized as follows: We describe the QG model and provide an overview of the wavelet method in Section 2. Results are given in Section 3 where we compare our wavelet spectra to the canonical Fourier spectra. Conclusions are given in Section 4.

2 Theory and technique

We describe the configuration of our quasi-geostrophic (QG) model and provide an overview of the wavelet method.

2.1 Description of the quasi-geostrophic simulation

We consider a stochastically forced two-layer QG flow in a doubly periodic f plane domain (i.e. $\beta = f_y = 0$) under rigid-lid and flat bottom conditions. Solutions to the QG potential vorticity (PV) equation

$$q_{j\,t} + J(\psi_j, q_j) = -r_b \nabla^2 \psi_j \delta_{j,2} + \mathcal{Q} \tag{1}$$

are computed using the psuedo-spectral `pyqg` model (Abernathey et al., 2022), where $\delta_{i,j}$ is the usual Kronecker delta function and layer numbers are denoted $j = 1, 2$. The linear bottom drag coefficient is $r_b = 5.787 \times 10^{-7}\,\mathrm{s}^{-1}$. The PV in each layer are

$$q_1 = \nabla^2\psi_1 + F_1(\psi_2 - \psi_1)\,, \tag{2}$$

$$q_2 = \nabla^2\psi_2 + F_2(\psi_1 - \psi_2)\,. \tag{3}$$

The vortex stretching coefficients are $F_1 = \frac{(2\pi/R_d)^2}{1+\delta}, F_2 = \delta F_1$ where the internal Rossby deformation radius was prescribed as $R_d = 100\,\mathrm{km}$. Each layer thickness is $(H_1, H_2) = (500, 2000)\,\mathrm{m}$ respectively, giving $\delta = H_1/H_2 = 0.25$. The square domain size is $L_0 = 1000\,\mathrm{km}$ with the spatial resolution of $\sim 2\,\mathrm{km}$ (512×512 grid points). In order to prevent the system from equilibrating to the well-known single pair of positive and negative vortices (Vallis, 2006), a vertically uniform forcing was introduced as

$$\mathcal{Q} = A_q w(t, z, y, x)\,, \tag{4}$$

where $A_q = 10^{-15}\,\mathrm{s}^{-2}$ is the amplitude and $w(t, z, y, x)$ is white noise in space-time with zero mean and $O(1)$ amplitude per layer (Fig. 1). The quantity $w(t, z, y, x)$ was computed by taking the inverse Fourier transform of a ring in wavenumber space

$$\hat{w}(t, z, l, k) = \begin{cases} a(t, l, k) + ib(t, l, k)\,, & \text{if } (R_d + \delta_R)^{-1} < \sqrt{k^2 + l^2} < (R_d - \delta_R)^{-1} \\ 0\,, & \text{otherwise} \end{cases}\,, \tag{5}$$

where a and b are Gaussian random variables with zero mean and standard deviation of unity in horizontal wavenumber space, and $\delta_R = 5\,\mathrm{km}$. In other words, the model is stochastically forced at scales about the Rossby radius. The model was spun up for 10 years from a state of rest, at which point area averaged energy had equilibrated (not shown), and then run for another 10 years with outputs saved every 10 days as instantaneous snapshots. No background PV was prescribed.

In this simple configuration, it is expected the flow will be both homogeneous and isotropic. Further, classical theory predicts the existence of an inverse cascade of KE and hence a $-5/3$ power law at scales larger than the forcing scale, and a forward cascade of enstrophy and hence -3 power law at smaller scales (Vallis, 2006). In this sense, we 'know' what the answer should be and can use the results to test the efficacy of the wavelet transform. The double periodicity also allows for a straightforward comparison between the wavelet and Fourier approach as no windowing of the data is necessary in applying the transforms. We exhibit the top- and bottom-layer PV at the last time step of the model output in Fig. 2.

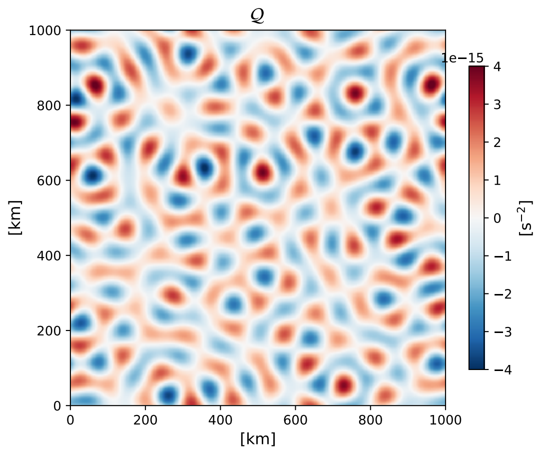

Figure 1. Example of how the vertically uniform stochastic forcing $\mathcal{Q}$ looks like for an arbitrary time step.

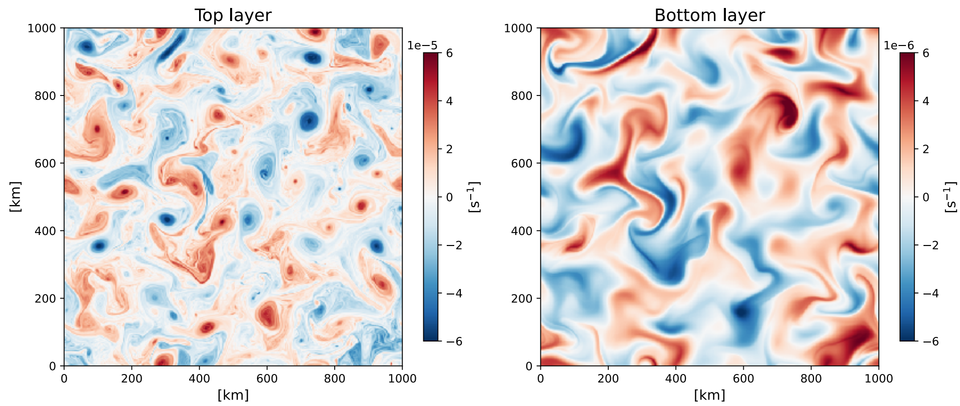

Figure 2. The PV at the last time step of the simulation outputs in the top and bottom layer. Note the order of magnitude difference in the two panels.

2.2 Spectral Considerations

For the reasons outlined in the introduction, we depart from the classical Fourier approach to compute wavenumber spectra, but do note the utility of that wavenumber spectrum emerges largely from Parseval's equality

$$\int_{\boldsymbol{x}} K(\boldsymbol{x})\, d\boldsymbol{x} = \int_{\boldsymbol{k}} \widehat{E}_K(\boldsymbol{k})\, d\boldsymbol{k}\,, \tag{6}$$

where K is kinetic energy (KE; e.g. Scott & Wang, 2005; Capet et al., 2008; Uchida et al., 2017). The Fourier energy spectrum is given by $2\widehat{E}_K(\boldsymbol{k}) = \hat{\boldsymbol{u}}^{*}\cdot\hat{\boldsymbol{u}}$ where the Fourier transform of the velocity is denoted by the hat ($\hat{\boldsymbol{u}}$) and the superscript * denotes the complex conjugate. This equivalence of the area integrated KE to the wavenumber integrated

Fourier spectrum motivates the latter's interpretation as the KE density in the wavenumber domain.

We base our spectral analysis on wavelet decompositions, rather than Fourier transforms, as the space-time locality of wavelets does not require the data to be periodic. Given a function dependent on two spatial dimensions, $f(\boldsymbol{x})$, its continuous wavelet transform is given by

$$\tilde{f}(s,\phi,\boldsymbol{\gamma}) = \int_\Omega f(\boldsymbol{x})\frac{1}{s}\xi^*(\mathsf{R}^{-1}\cdot\left(\frac{\boldsymbol{x}-\boldsymbol{\gamma}}{s}\right))\,d\boldsymbol{x}\,, \tag{7}$$

where the integration is taken over the whole domain of interest Ω and R^{-1} is the inverse of the rotation matrix

$$\mathsf{R}^{-1} = \begin{pmatrix} \cos(\phi) & \sin(\phi) \\ -\sin(\phi) & \cos(\phi) \end{pmatrix}, \tag{8}$$

for rotation through an angle ϕ. The quantity s is referred to as the 'scale', $\boldsymbol{\gamma}\,(\in\ R^2)$ are the two-dimensional coordinates of interest, $\xi(\boldsymbol{x})$ is the so-called 'mother' wavelet and $\xi(\mathsf{R}^{-1}\cdot(\boldsymbol{x}-\boldsymbol{\gamma})\,/s)$ in (7) the daughter wavelets. The quantities $\tilde{f}$ are called the wavelet coefficients. Note that the field of wavelet coefficients is a filtered version of the original data.

Subject to the 'admissibility condition' $C_\Xi < \infty$, the original function f can be reconstructed from the wavelet coefficients

$$f(\boldsymbol{x}) = \frac{1}{C_\Xi}\int_{\boldsymbol{\gamma}}\int_s\int_\phi \tilde{f}(s,\phi,\boldsymbol{\gamma})\frac{1}{s^4}\xi(\mathsf{R}^{-1}\cdot\left(\frac{\boldsymbol{x}-\boldsymbol{\gamma}}{s}\right))\,d\phi\,ds\,d\boldsymbol{\gamma}\,. \tag{9}$$

If $\hat{\Xi}(\boldsymbol{k})$ is the Fourier transform of the mother wavelet, then

$$C_\Xi = \int_{\boldsymbol{k}}\frac{\hat{\Xi}^*\hat{\Xi}}{\boldsymbol{k}\cdot\boldsymbol{k}}\,d\boldsymbol{k}\,. \tag{10}$$

The so-called 'admissibility condition' implies that the mother wavelet defines a well-behaved class of wavelet transforms. Many functions satisfy (10) provided they have zero mean

$$\int_{\boldsymbol{x}}\xi(\boldsymbol{x})d\boldsymbol{x} = 0\,. \tag{11}$$

For current purposes, we will employ the so-called Morlet wavelet (Morlet et al., 1982; Gabor, 1946), i.e.

$$\xi(\boldsymbol{x}) = \left(e^{-2\pi i\boldsymbol{k}_0\cdot\boldsymbol{x}} - c_0\right)e^{-\frac{\boldsymbol{x}\cdot\boldsymbol{x}}{2x_0^2}}\,, \tag{12}$$

where c_0 is a constant included to insure that (11) is met. The central wavenumber $\boldsymbol{k}_0$ is taken to be $\boldsymbol{k}_0 = (k_0, 0)$ and the quantity x_0 is a reference length scale, here taken to be the Rossby radius ($x_0 = 100\,\text{km}$), viz. the central length scale of the mother wavelet. We will choose $k_0 = 1/x_0$, in which case the constant c_0 is quite small and generally ignored (i.e. $c_0 = 0$), a convention adopted in this paper. Plots of (12) are found in Fig. 3. Note that the Morlet mother wavelet consists of a wave of wavelength x_0 inside a Gaussian envelope of decay scale $\sqrt{2}x_0$. Thus for $s = 1$ and $\phi = 0$, the wavelet coefficient produced by this transformation comments on the presence of the wavenumber $\boldsymbol{k}_0 = (k_0, 0)$ at location $\boldsymbol{\gamma}$ in the original data. Increasing the rotation angle ϕ and filtering returns information about the presence of the same wavelength at angle $-\phi$. Finally allowing s to vary modifies the filter so that the primary wavelength of the filter is $k = 1/(sx_0)$. The Morlet wavelet coefficient can thus be thought of as a 'local' Fourier transform at wavenumber $\boldsymbol{k}_0^{\mathsf{T}} \cdot \mathsf{R}^{-1}(\phi)/s$, where the superscript T denotes a transpose.

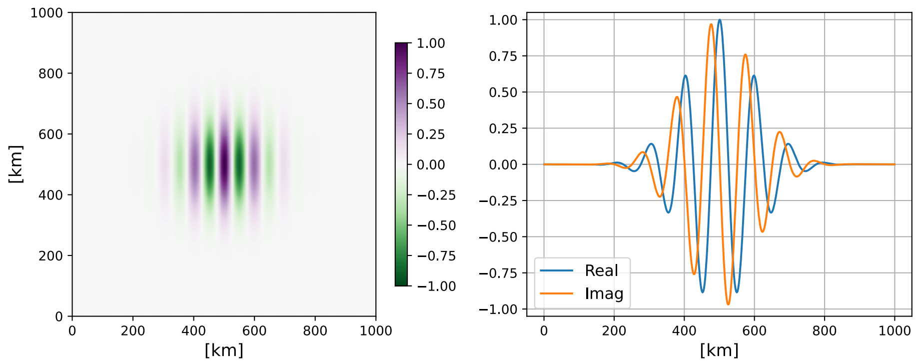

Figure 3. Structure of the mother Morlet wavelet (12) for $c_0 = 0$. A contour plot of the real part of the mother Morlet wavelet is shown in the left panel. Zonal transects of the real and imaginary parts at $y = 500\,\text{km}$ appear in the right panel. The reference lengthscale is $x_0 = 100\,\text{km}$.

From the properties of wavelets, it is possible to show they satisfy a generalized Parseval's equality (cf. Appendix A), namely

$$\int_{\boldsymbol{x}} f(\boldsymbol{x}) g(\boldsymbol{x}) d\boldsymbol{x} = \frac{1}{C_\Xi} \int_\phi \int_s \int_{\boldsymbol{\gamma}} \frac{\tilde{f}\tilde{g}^*}{s^3}\, d\boldsymbol{\gamma}\, ds\, d\phi\,. \tag{13}$$

Note, if $f = g$, then the variance in f is captured via

$$\int_{\boldsymbol{x}} f^2(\boldsymbol{x}) d\boldsymbol{x} = \frac{1}{C_\Xi} \int_\phi \int_s \int_{\boldsymbol{\gamma}} \frac{\tilde{f}^*\tilde{f}}{s^3}\, d\boldsymbol{\gamma}\, ds\, d\phi\,, \tag{14}$$

which identifies the quantity

$$\widetilde{E}_S(\boldsymbol{\gamma}, \phi, s) = \frac{1}{C_\Xi} \frac{\tilde{f}^*\tilde{f}}{s^3}\,, \tag{15}$$

as the energy density of f in wavelet space s. In other words, Eq. (15) gives a spectral energy estimate for f that belongs to location $\boldsymbol{\gamma}$.

At this point, the scale factor in (15), s, is non-dimensional. It is more traditional in fluid mechanics to discuss energy spectra in terms of wavenumber. As pointed out above, the effective wavenumber associated with s is $k = 1/(sx_0) = 1/s_0$, where the quantity s_0 has units of length. One can transform (14) from s to s_0 space as

$$\int_{\boldsymbol{x}} f^2(\boldsymbol{x})d\boldsymbol{x} = \frac{1}{C_\Xi}\int_\phi\int_{s_0}\int_{\boldsymbol{\gamma}} \frac{\tilde{f}^*\tilde{f}}{s_0^3}x_0^2\,d\boldsymbol{\gamma}\,ds_0\,d\phi\,, \tag{16}$$

and finally to wavenumber, $k = 1/s_0$, space, ending with

$$\int_{\boldsymbol{x}} f^2(\boldsymbol{x})d\boldsymbol{x} = \frac{1}{C_\Xi}\int_\phi\int_{k}\int_{\boldsymbol{\gamma}} \tilde{f}^*\tilde{f}x_0^2k\,d\boldsymbol{\gamma}\,dk\,d\phi\,. \tag{17}$$

If we now produce wavelet coefficients for the stream function and PV from time step n of our simulation, and manipulate them appropriately, we obtain

$$\widetilde{E}_K^n(\boldsymbol{\gamma},\phi,k) = \frac{1}{C_\Xi}\mathcal{R}\left[(-\tilde{\psi}^*)\tilde{q}\right]x_0^2k\,, \tag{18}$$

$$\widetilde{Z}_K^n(\boldsymbol{\gamma},\phi,k) = \frac{1}{C_\Xi}\mathcal{R}\left[\frac{\tilde{q}^*\tilde{q}}{2}\right]x_0^2k\,, \tag{19}$$

where $\mathcal{R}[\cdot]$ is the real part of the quantity $\cdot$, as a measure of energy and enstrophy density in wavelet transform space (cf. Vallis, 2006; Uchida, Deremble, & Penduff, 2021). Each value of $\widetilde{E}_K^n$ and $\widetilde{Z}_K^n$ is a random number. Averaging those values, here taken as a temporal averaging of them every 30 days, returns an estimate of the energy spectrum as a function of wavenumber k in direction ϕ. The interval of 30 days ensures temporal decorrelation between the density estimates. The spatial locality of the mother wavelet permits the interpretation of $\widetilde{E}_K(\boldsymbol{\gamma},\phi,k) = \overline{\widetilde{E}_K^n(\boldsymbol{\gamma},\phi,k)}$ as the local energy spectrum at location $\boldsymbol{\gamma}$. The same argument applies for enstrophy.

3 Results

We have opted for this work to calculate the wavelet coefficients explicitly, rather than by the frequently used Fourier transform method, in view of our eventual interest in applications to realistic aperiodic and inhomogeneous settings, such as the North Atlantic basin. The wavelet transform appropriate to the angle ϕ was taken between $[0, -\pi)$ with the azimuthal resolution of $\pi/12$ radian $(= 15^\circ)$. The sum of the product of the wavelet and the data spatially integrated is the wavelet coefficient at the location $\boldsymbol{\gamma}$. In what follows, we consider the quasi two-dimensional flow in the top layer ($j = 1$).

3.1 Spectra over the entire domain

We examine and intercompare the wavelet and Fourier wavenumber spectra and spectral flux over the entire domain in this section. As the simulated domain is doubly periodic and on a uniform grid, it is an ideal case for the Fourier method; no windowing nor spatial interpolation are applied prior to taking the transform. Although one of the strengths of the wavelet approach is in negating the necessity of periodicity, we have chosen such an idealized configuration to test the wavelet method against the Fourier method where the latter would provide the "true" spectra.

While the scaling factor s provides flexibility in defining the wavelet wavenumber, as opposed to the Fourier approach where, to employ Fast Fourier Transform algorithms, the resolution is constrained to $1/L$ with $L\,(=1000\,\text{km})$ being the domain size, we start by computing the wavelet spectra at the center location $\boldsymbol{\gamma} = \boldsymbol{\gamma}_0 = (y_c, x_c) = (500, 500)\,\text{km}$ and use the same wavenumbers as the Fourier spectra (k_F). We see from Fig. 4 that the agreement between the Fourier and wavelet method is excellent (red solid and black dashed curves respectively) for both the energy and enstrophy spectra.

We also show in Fig. 4 a case where we increase the wavelet wavenumber resolution at scales larger than the Rossby radius where the inverse cascade is expected (cyan dotted curve); we take $s_0 = [2\Delta x, ..., 5x_0]$ monotonically spaced with 50 increments. Features at the lowest wavenumbers (i.e. largest spatial scales) are better captured compared to the red solid and black dashed curves in Fig. 4 where the Fourier wavenumber resolution is low. This is beneficial as the inertial range associated with a $-5/3$ power law is expected at length scales larger than the Rossby radius; a plateau at scales around $k \sim 7{\times}10^{-3}$ cpkm can be seen in the cyan dashed line in Fig. 4b. Although the monotonic spacing in s results in lower resolution at higher wavenumbers, we note that one may arbitrarily increase the wavenumber resolution across all scales. The enstrophy spectra are slightly steeper than k^{-1} at scales below the Rossby radius (Fig. 4c,d), and is consistent with the KE spectral slope also being steeper than -3. We attribute the steeper slope to the excessive PV variance introduced by the stochastic forcing cascading downscale (cf. Fig. 5b). The spectral slopes have been shown to be sensitive to the model configuration of forcing and dissipation (Maltrud & Vallis, 1991), but this does not diminish the agreement between the Fourier and wavelet spectral estimates.

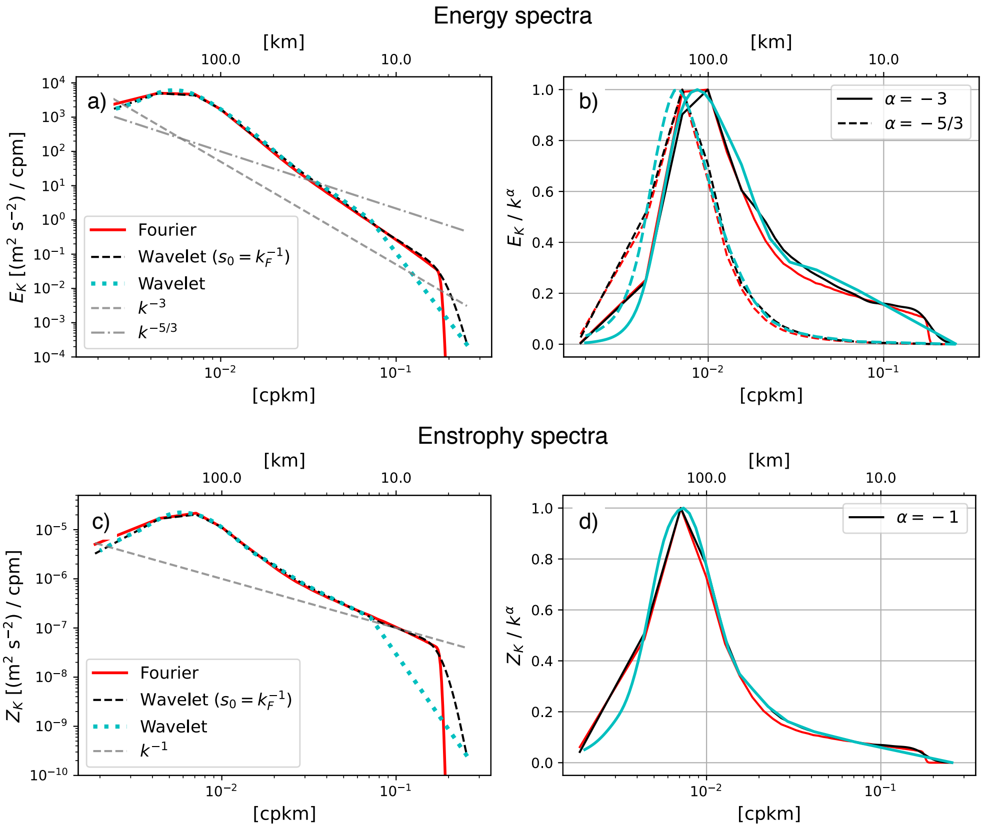

Figure 4. The isotropic (azimuthally-integrated) energy and enstrophy wavenumber spectra of the top layer (a,c). For the wavelet approach, spectra at $\gamma = \gamma_0$ where the wavenumbers are identical to the Fourier wavenumbers ($s_0 = k_F^{-1}$; black dashed) and where the wavenumber resolution is increased at small wavenumbers (cyan dotted) are given. The right column exhibits the isotropic (azimuthally-integrated) spectra normalized by the -3 and $-5/3$ power law for energy and -1 for enstrophy (b,d). The colors correspond to red being the Fourier and black the wavelet approach with identical wavenumbers with the Fourier and cyan with the wavenumber resolution increased at lower wavenumbers. The wavenumber are shown in the lower x axes and corresponding lengthscale in the upper axes.

Using the wavelet transformation, we can also diagnose the kinetic energy (KE) and enstrophy spectral flux as

$$\tilde{\varepsilon}_K(\boldsymbol{\gamma}, \phi, k) = -\frac{1}{C_\Psi} \int_{k>\kappa} \mathcal{R}\left[\overline{\tilde{u}^*(\widetilde{\boldsymbol{u}\cdot\nabla u})} + \overline{\tilde{v}^*(\widetilde{\boldsymbol{u}\cdot\nabla v})}\right] x_0^2 \kappa \, d\kappa \,, \tag{20}$$

$$\tilde{\eta}_K(\boldsymbol{\gamma}, \phi, k) = -\frac{1}{C_\Psi} \int_{k>\kappa} \mathcal{R}\left[\overline{\tilde{q}^*(\widetilde{\boldsymbol{u}\cdot\nabla q})}\right] x_0^2 \kappa \, d\kappa \,, \tag{21}$$

where negative values imply a inverse cascade towards larger scales and positive values a forward cascade towards smaller scales (Arbic et al., 2013; Khatri et al., 2018). Figure 5a,b exhibits the well documented inverse KE cascade ($\varepsilon_K < 0$) at scales larger than the Rossby radius and forward enstrophy cascade ($\eta_K > 0$) at scales smaller than the Rossby radius. The lower panels in Fig. 5 show the azimuthally-integrated spectral transfers, i.e. the integrand of (20) and (21).

We note that the wavelet spectral flux is sensitive to the wavenumber resolution, particularly for the enstrophy flux (black dotted and dashed curves in Fig. 5b). This sensitivity arises because the flux is the transfer cumulatively integrated from the largest wavenumbers towards smaller wavenumbers (i.e. (20)) so values at high wavenumbers can have a substantial effect on the flux at low wavenumbers. In this case, we expect the 'correct' answer to reflect theoretical inertial regime predictions. The wavelet diagnosed enstrophy flux fails this test in that it predicts an upscale enstrophy cascade (black dashed curve in Fig. 5b), counter to that computed from the Fourier approach. While the Fourier estimate provides a constant flux of enstrophy around $0.44 \times 10^{-17}\,\mathrm{s}^{-3}$ across a wide range of wavenumbers (red curve in Fig. 5b), the wavelet estimate exhibits a more wavenumber-dependent enstrophy flux. We argue this wavenumber dependency is associated with the fact that the wavelet estimate of the spectral transfer only incorporates spatially local information while the Fourier approach effectively yields a domain-averaged estimate. Namely, the global two-point correlation function, stemming from the assumption of homogeneity in the Fourier approach, virtually acts as a spatial averaging operator (cf. Uchida, Jamet, et al., 2021). For this setting, this assumption is valid, hence the superior performance in flux estimation of the Fourier approach. Note, however, that the transfer estimates emerging from the wavelet approach, while noisy, do largely agree with those of the Fourier approach. It is in the integration of the transfers that initial noise in the estimates can result in an erroneous outcome. The expectation is that if we were to take the explicit wavelet transform at every single grid point, the spatial average of the wavelet spectral flux would converge to the Fourier approach. We examined this by estimating the wavelet spectral flux and transfer at every five grid points in the diagonal direction (i.e. every $\sim 14\,\mathrm{km}$) up to 100 grid points apart ($\sim 280\,\mathrm{km}$) from the center point (79 locations in total along $y - y_c = \pm(x - x_c)$). The spatial average of them shown as cyan curves in Fig. 5 all come closer to the Fourier estimate than the black curves. The reduction in magnitude of the wavelet KE spectral flux, for example, stems from the fact that at some locations, there were local pockets of forward KE cascade at scales about the Rossby radius and larger ($\tilde{\varepsilon}_K > 0$; not shown).

We are thus led to be cautious in interpreting wavelet spectral calculations when applied to what might be termed higher order quantities, like spectral flux. However, we also point out this is a sword that cuts in both directions. The accuracy of the Fourier flux estimates depends strongly on their area wide integrative effect in this homogeneous setting. However, were the flow not homogeneous, the integrative character of the Fourier approach would obscure the meaning of the result.

We end this section by showing the local anisotropies in the flow, which the wavelet approach can extract via its dependence on the angle ϕ (Fig. 6). The flux shown in Fig. 5a,b are the azimuthal integration of Fig. 6. As expected from Fig. 5, the signal of anisotropy at $\boldsymbol{\gamma} = \boldsymbol{\gamma}_0$ (left panels of Fig. 6) is larger than when the flux is spatially averaged ($\langle\boldsymbol{\gamma}\rangle$; right panels of Fig. 6). As the simulated QG flow is configured to be isotropic in the spatially averaged sense, the spectral flux converging towards isotropy is comforting to see. Nevertheless, the convergence towards isotropy upon spatial averaging implies that the angular dependence of the flux is location dependent and the isotropy that emerges from the Fourier estimate is not expected to hold locally in the spatial domain.

3.2 Spectra over a non-periodic subdomain

We now examine the spectra taken over the subdomain given by $y = 200\text{-}800\,\mathrm{km}$ and $x = 200\text{-}800\,\mathrm{km}$ in anticipation of realistic data where periodicity is never satisfied. As the data is no longer periodic, the Fourier approach requires the data to be windowed. This will highlight the strength of the locality in the wavelet approach where windowing of the data is unnecessary. Prior to taking the Fourier transforms, we applied Hann windows (Arbic et al., 2013; Uchida et al., 2017; Uchida, Jamet, et al., 2021) and then corrected for their amplitude. Comparing Figs. 4 and 7, we see that the spectral estimates are still robust. The low resolution at lower wavenumbers from the Fourier method

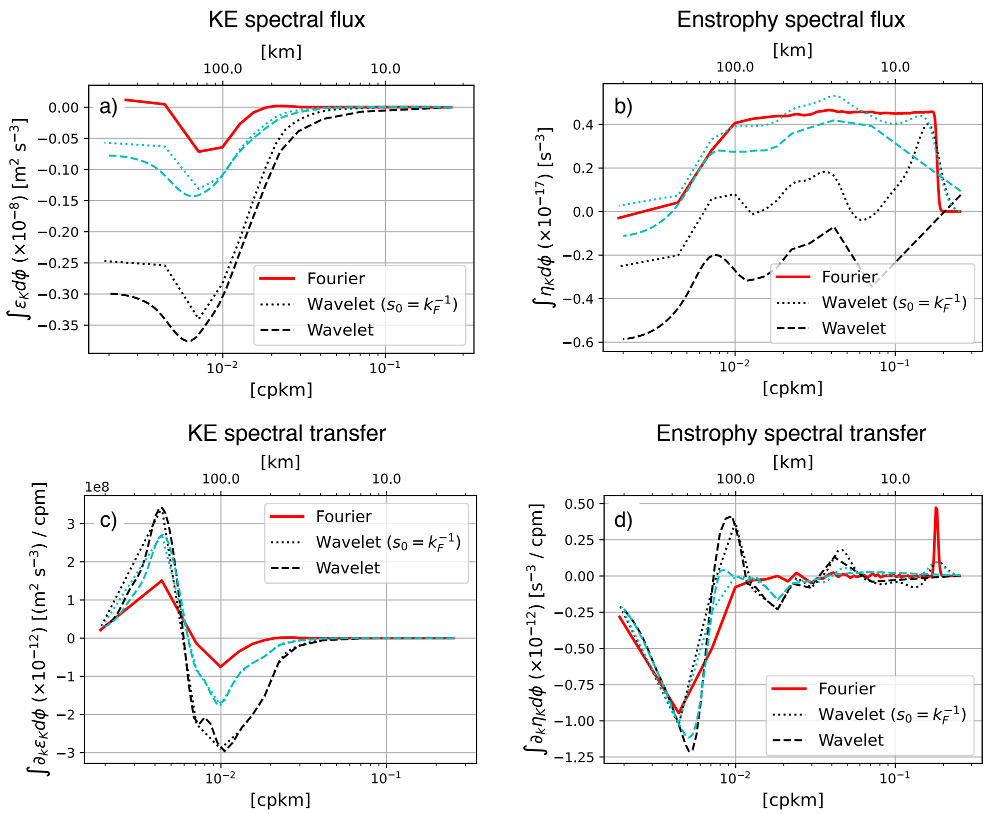

Figure 5. The isotropic (azimuthally integrated) KE and enstrophy wavenumber spectral flux (a,b) and transfer (c,d) respectively. The Fourier method is shown in red and the wavelet approach at $\boldsymbol{\gamma} = \boldsymbol{\gamma}_0$ with wavenumbers identical to the Fourier wavenumbers in dotted ($s_0 = k_F^{-1}$) and the case with increased wavenumber resolution at smaller wavenumbers in dashed curves respectively. The black curves show the wavelet flux and transfer at $\boldsymbol{\gamma} = \boldsymbol{\gamma}_0$, while the cyan curves show them averaged over the 79 locations ($\langle \boldsymbol{\gamma} \rangle$). The wavenumber are shown in the lower x axes and corresponding lengthscale in the upper axes.

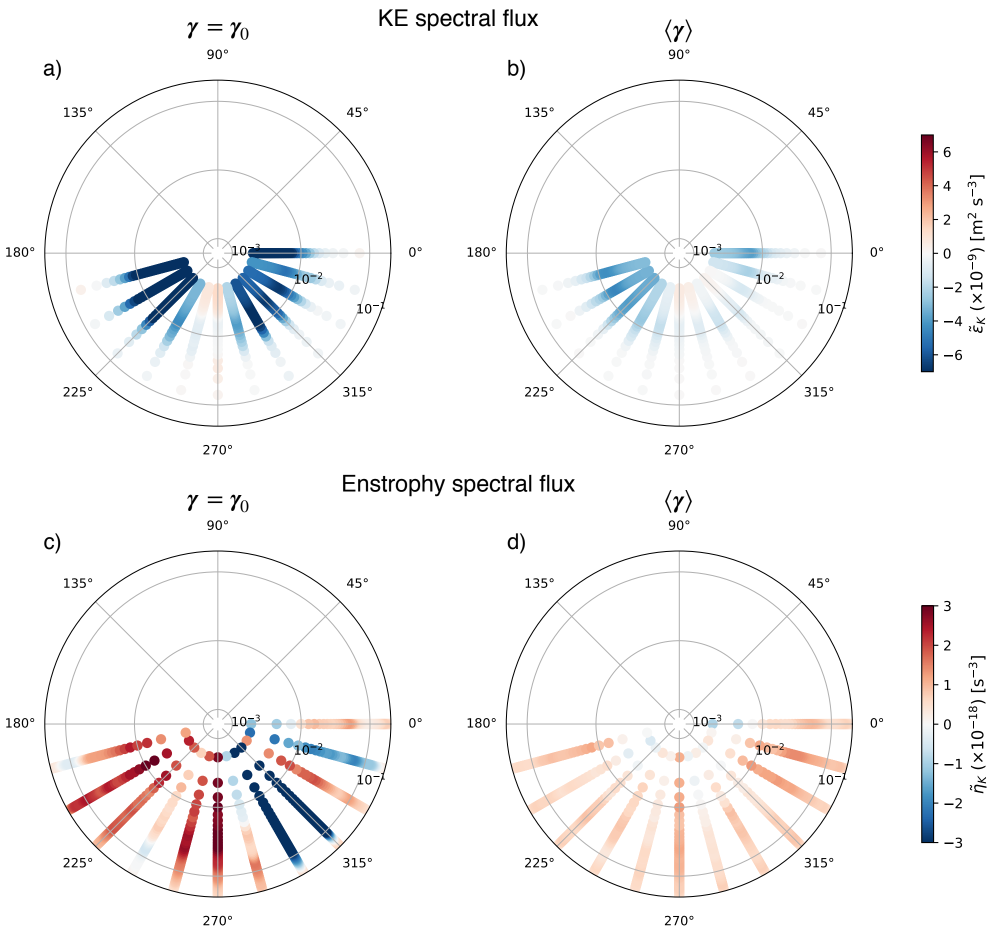

Figure 6. The angular dependence of the KE and enstrophy spectral flux from the wavelet approach plotted radially (a,b). The radial axes are the wavenumbers in logarithmic scaling. The KE flux has the wavenumber resolution increased at small wavenumbers and enstrophy flux with identical wavenumbers as the Fourier method ($s_0 = k_F^{-1}$) as the inverse KE cascade occurs at lower wavenumbers while as the forward enstrophy cascade occurs at higher wavenumbers. The left panels are for estimates at $\boldsymbol{\gamma} = \boldsymbol{\gamma}_0$ while the right panels are the average over 79 locations $\langle\boldsymbol{\gamma}\rangle$.

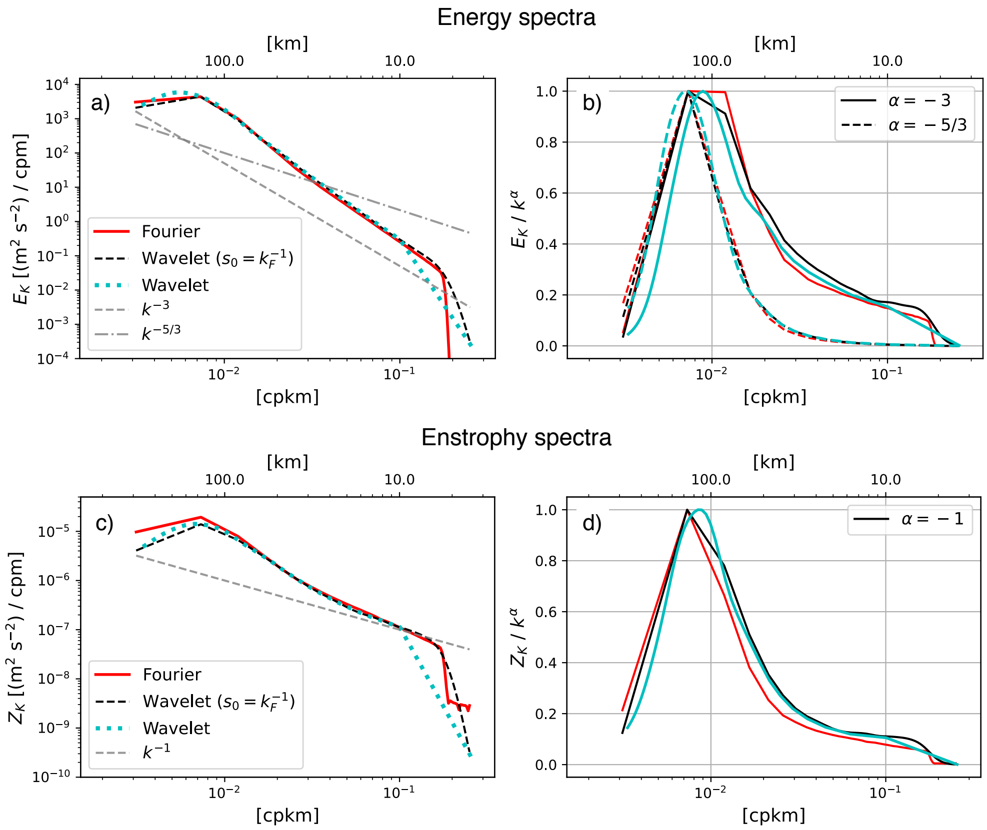

Figure 7. Same as Fig. 4 but for the subdomain of $y = 200$ - 800 km and $x = 200$ - 800 km.

287 makes it difficult to detect the $k^{-5/3}$ power law due to the domain size being small; there are only two wavenumber points at scales larger than the Rossby radius (red curves in Fig. 7). The wavelet approach, on the other hand through its flexibility in s, still captures the power law around $k \sim 7 \times 10^{-3}$ cpkm (cyan curves in Fig. 7a,b); the scaling for the wavelet approach was adjusted to $s_0 = [2\Delta x, ..., 3x_0]$ over 50 monotonic increments in order to account for the smaller domain.

Regarding the spectral transfer, the Fourier approach is affected by the tapering at the lowest wavenumbers (red curves in Figs. 5c,d and 8c,d) but the wavelet approach is still able to capture the change in sign in the curvature (black dashed curves in Figs. 5c,d and 8c,d).

4 Conclusions and discussion

In this study, we have described and documented a wavelet-based technique for spectral analyses. The wavelet approach employed here, through its dependence on a scale

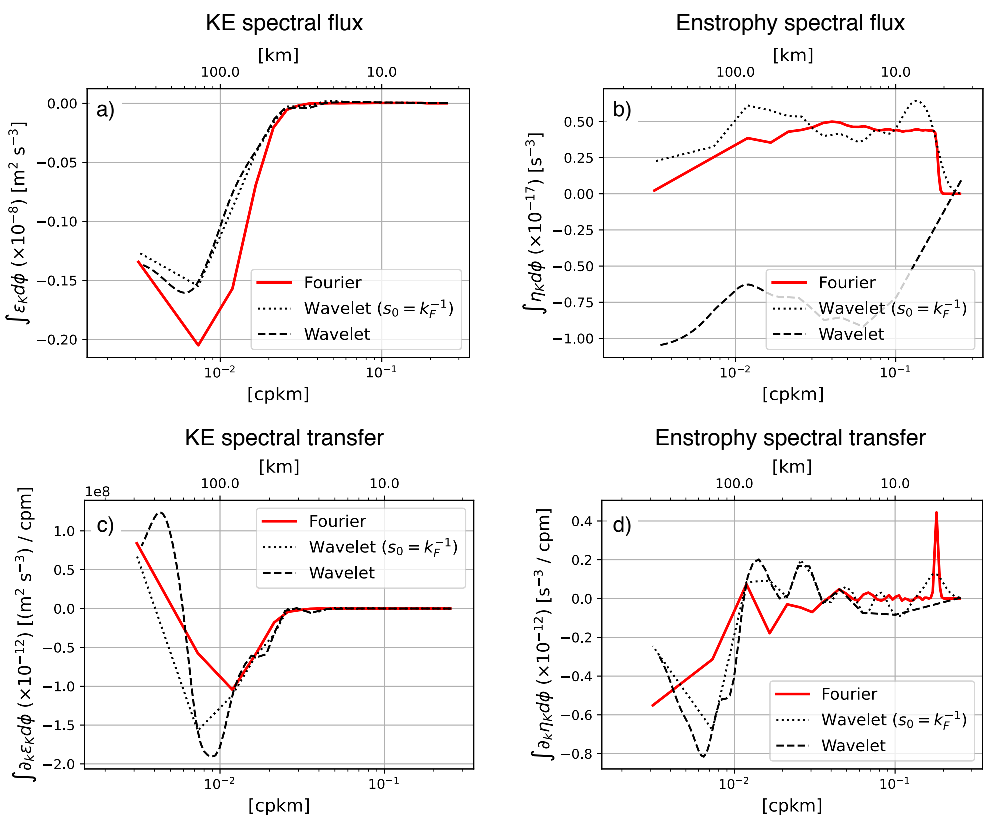

Figure 8. Same as Fig. 5 but for the subdomain of $y = 200$ - 800 km and $x = 200$ - 800 km. (We do not show spatially averaged spectral flux and transfer for the wavelet approach.)

parameter s, returns effectively a one-dimensional (1D) spectral estimate. While this is analogous to 1D along-track Fourier spectral estimates using 1D data such as ship-track observations where the axis of transformation is aligned with the ship-track orientation (e.g. Callies & Ferrari, 2013), the wavelet approach incorporates two-dimensional data allowing for information regarding anisotropy through its angular dependency (Fig. 6).

We have demonstrated its utility by applying it to a doubly-periodic, two-layer, quasi-geostrophic (QG) simulation. The flow analyzed in this study is highly idealized being spatially isotropic and homogenous. The idealized setting, however, is expected to yield known wavenumber spectral slopes (i.e. $-5/3$ in the inverse KE cascade range and -3 in the forward enstrophy cascade range), so it can be used as a test bed for the wavelet approach. The agreement between the wavelet and Fourier approach, particularly for the spectra (Figs. 4 and 7), encourages the usage of wavelets with its additional strengths of being able to capture the local features of the flow. The wavelet approach negating the necessity for the data to be periodic is another benefit for realistic settings such as the North Atlantic basin. The robustness of the spectra is comforting, but we also emphasize the need for caution when computing higher order spectral quantities, like spectral fluxes.

Our work is complementary to recent work by Aluie et al. (2018) and Sadek and Aluie (2018) where they use a spatial filter to examine the KE spectra and cross-scale transfer, Jamet et al. (2020) where they employ the Green's function, and Uchida, Jamet, et al. (2021) where they use Empirical Orthogonal Functions. Notably, San Liang (2016) and Yang et al. (2021) are interesting attempts to examine the energy exchange across spatiotemporal scales by decomposing the flow with a set of orthonormal wavelet bases. Here, we have documented the cross-scale energetics in the spectral context.

Acknowledgments

This study is a contribution to the 'Assessing the Role of forced and internal Variability for the Ocean and climate Response in a changing climate' (ARVOR) project supported by the French 'Les Enveloppes Fluides et l'Environnement' (LEFE) program. This work was supported via NSF grants OCE-1829856, OCE-2023585, OCE-2123632 and the French 'Make Our Planet Great Again' (MOPGA) program managed by the Agence Nationale de la Recherche under the Programme d'Investissement d'Avenir, reference ANR-

18-MPGA-0002. The latter grant served as the primary support for T. Uchida and partially for Q. Jamet. We would like to thank Edward Peirce and Kelly Hirai for maintaining the Florida State University cluster on which the simulations were run and data were analyzed.

Data availability statement

The wavelet transforms were taken using the `xwavelet` Python package (Uchida & Dewar, 2022) and Fourier transforms using the `xrft` Python package (Uchida et al., 2022). Jupyter notebooks used to run the `pyqg` simulation and conduct analyses are available via Github (`https://github.com/roxyboy/QG-wavelets`; a DOI will be added upon acceptance of the manuscript).

Appendix A Parseval's equality

In this appendix, we show the Parseval's equality for two-dimensional wavelet transforms, i.e.

$$\int f\, g\, d\boldsymbol{x} = \frac{1}{C_\Xi} \iiint \tilde{f}\, \tilde{g}^* \frac{1}{s^3}\, d\boldsymbol{\gamma} ds d\phi\,. \tag{A1}$$

Using (9), the right-hand side can be expanded as

$$\begin{aligned}\iiint \tilde{f}\, \tilde{g}^* \frac{1}{s^3}\, d\boldsymbol{\gamma} ds d\phi &= \iiint \frac{1}{s^5} \int_{\boldsymbol{x}} f(\boldsymbol{x}) \xi^*(\mathsf{R}^{-1} \cdot \left(\frac{\boldsymbol{x}-\boldsymbol{\gamma}}{s}\right)) d\boldsymbol{x} \int_{\boldsymbol{\chi}} g^*(\boldsymbol{\chi}) \xi(\mathsf{R}^{-1} \cdot \left(\frac{\boldsymbol{\chi}-\boldsymbol{\gamma}}{s}\right)) d\boldsymbol{\chi}\, d\boldsymbol{\gamma} ds d\phi \\ &= \int_{\boldsymbol{x}} \int_{\boldsymbol{\chi}} \frac{f\, g^*}{s^5} \iiint \xi^*(\mathsf{R}^{-1} \cdot \left(\frac{\boldsymbol{x}-\boldsymbol{\gamma}}{s}\right)) \xi(\mathsf{R}^{-1} \cdot \left(\frac{\boldsymbol{\chi}-\boldsymbol{\gamma}}{s}\right))\, d\boldsymbol{\gamma} ds d\phi\, d\boldsymbol{x}\, d\boldsymbol{\chi}\,.\end{aligned} \tag{A2}$$

Now, consider the wavelet transform of the Dirac delta function

$$\begin{aligned}\tilde{\delta} &= \int_{\boldsymbol{x}} \delta(\boldsymbol{x}-\boldsymbol{y}) \frac{1}{s} \xi^*(\mathsf{R}^{-1} \cdot \left(\frac{\boldsymbol{x}-\boldsymbol{\gamma}}{s}\right))\, d\boldsymbol{x} \\ &= \frac{1}{s} \xi^*(\mathsf{R}^{-1} \cdot \left(\frac{\boldsymbol{y}-\boldsymbol{\gamma}}{s}\right))\,.\end{aligned} \tag{A3}$$

Hence, the inverse wavelet transform becomes

$$\begin{aligned}\delta &= \frac{1}{C_\Xi} \iiint \tilde{\delta} \frac{1}{s^4} \xi(\mathsf{R}^{-1} \cdot \left(\frac{\boldsymbol{x}-\boldsymbol{\gamma}}{s}\right))\, d\phi ds d\boldsymbol{\gamma} \\ &= \frac{1}{C_\Xi} \iiint \frac{1}{s^5} \xi^*(\mathsf{R}^{-1} \cdot \left(\frac{\boldsymbol{y}-\boldsymbol{\gamma}}{s}\right)) \xi(\mathsf{R}^{-1} \cdot \left(\frac{\boldsymbol{x}-\boldsymbol{\gamma}}{s}\right))\, d\phi ds d\boldsymbol{\gamma}.\end{aligned} \tag{A4}$$

Plugging (A4) into (A2) yields

$$\iiint \tilde{f}\, \tilde{g}^* \frac{1}{s^3}\, d\boldsymbol{\gamma} ds d\phi = C_\Xi \int_{\boldsymbol{x}} f\, g^*\, d\boldsymbol{x}\,, \tag{A5}$$

and we obtain (A1).

References

Abernathey, R. P., Ross, A., Jansen, M., Li, Z., Poulin, F. J., Constantinou, N. C., ... Bueti, M. (2022). `pyqg`*: Python quasigeostrophic model.* doi: 10.5281/zenodo.6563667

Aluie, H., Hecht, M., & Vallis, G. (2018). Mapping the energy cascade in the North Atlantic Ocean: The coarse-graining approach. *Journal of Physical Oceanography*, *48*, 225-244. doi: 10.1175/JPO-D-17-0100.1

Arbic, B. K., Polzin, K. L., Scott, R. B., Richman, J. G., & Shriver, J. F. (2013). On eddy viscosity, energy cascades, and the horizontal resolution of gridded satellite altimeter products. *Journal of Physical Oceanography*, *43*(2), 283–300. doi: 10.1175/JPO-D-11-0240.1

Callies, J., & Ferrari, R. (2013). Interpreting energy and tracer spectra of upper-ocean turbulence in the submesoscale range (1–200 km). *Journal of Physical Oceanography*, *43*(11), 2456–2474. doi: 10.1175/JPO-D-13-063.1

Capet, X., McWilliams, J. C., Molemaker, M. J., & Shchepetkin, A. F. (2008). Mesoscale to submesoscale transition in the california current system. Part I: Flow structure, eddy flux, and observational tests. *Journal of physical oceanography*, *38*(1), 29–43. doi: 10.1175/2007JPO3671.1

Charney, J. G. (1971). Geostrophic turbulence. *Journal of the Atmospheric Sciences*, *28*(6), 1087–1095. doi: 10.1175/1520-0469(1971)028⟨1087:GT⟩2.0.CO;2

Gabor, D. (1946). Theory of communication. Part 1: The analysis of information. *Journal of the Institution of Electrical Engineers-Part III: Radio and Communication Engineering*, *93*(26), 429–441. doi: 10.1049/ji-3-2.1946.0074

Jamet, Q., Ajayi, A., Le Sommer, J., Penduff, T., Hogg, A., & Dewar, W. (2020). On energy cascades in general flows: A lagrangian application. *Journal of Advances in Modeling Earth Systems*, *12*(12), e2020MS002090. doi: 10.1029/2020MS002090

Jamet, Q., Deremble, B., Wienders, N., Uchida, T., & Dewar, W. K. (2021). On wind-driven energetics of subtropical gyres. *Journal of Advances in Modelling Earth Systems*, e2020MS002329. doi: 10.1029/2020MS002329

Khatri, H., Sukhatme, J., Kumar, A., & Verma, M. K. (2018). Surface ocean enstrophy, kinetic energy fluxes, and spectra from satellite altimetry. *Journal of Geophysical Research: Oceans*, *123*(5), 3875–3892. doi: 10.1029/2017JC013516

Kolmogorov, A. (1941). The local structure of turbulence in incompressible viscous fluid for very large Reynolds numbers. *C R Academy of Sciences URSS*, *30*, 301-305.

Maltrud, M., & Vallis, G. (1991). Energy spectra and coherent structures in forced two-dimensional and beta-plane turbulence. *Journal of Fluid Mechanics*, *228*, 321–342. doi: 10.1017/S0022112091002720

Morlet, J., Arens, G., Fourgeau, E., & Glard, D. (1982). Wave propagation and sampling theory—Part I: Complex signal and scattering in multilayered media. *Geophysics*, *47*(2), 203–221. doi: 10.1190/1.1441328

Nastrom, G., & Gage, K. (1983). A first look at wavenumber spectra from GASP data. *Tellus A*, *35*(5), 383–388. doi: 10.1111/j.1600-0870.1983.tb00213.x

Perrier, V., Philipovitch, T., & Basdevant, C. (1995). Wavelet spectra compared to Fourier spectra. *Journal of mathematical physics*, *36*(3), 1506–1519. doi: 10.1063/1.531340

Sadek, M., & Aluie, H. (2018). Extracting the spectrum of a flow by spatial filtering. *Physical Review Fluids*, *3*(12), 124610. doi: 10.1103/PhysRevFluids.3.124610

San Liang, X. (2016). Canonical transfer and multiscale energetics for primitive and quasigeostrophic atmospheres. *Journal of the Atmospheric Sciences*, *73*(11), 4439–4468. doi: 10.1175/JAS-D-16-0131.1

Scott, R., & Wang, F. (2005). Direct evidence of an oceanic inverse kinetic energy cascade from satellite altimetry. *Journal of Physical Oceanography*, *35*, 1650-1666. doi: 10.1175/JPO2771.1

Taylor, G. (1938). The spectrum of turbulence. *Proc. R. Soc. Lond. A1*, *164*, 476–490. doi: https://doi.org/10.1098/rspa.1938.0032

Torrence, C., & Compo, G. P. (1998). A practical guide to wavelet analysis. *Bulletin of the American Meteorological society*, *79*(1), 61–78. doi: 10.1175/1520-0477(1998)079⟨0061:APGTWA⟩2.0.CO;2

Uchida, T., Abernathey, R. P., & Smith, K. S. (2017). Seasonality of eddy kinetic energy in an eddy permitting global climate model. *Ocean Modelling*, *118*, 41–58. doi: 10.1016/j.ocemod.2017.08.006

Uchida, T., Deremble, B., & Penduff, T. (2021). The seasonal variability of the ocean energy cycle from a quasi-geostrophic double gyre ensemble. *Fluids*, *6*(6), 206. doi: 10.3390/fluids6060206

Uchida, T., & Dewar, W. K. (2022). `xwavelet`*: Wavelet transforms for xarray data.* doi: 10.5281/zenodo.6022738

Uchida, T., Jamet, Q., Poje, A., & Dewar, W. K. (2021). An ensemble-based eddy and spectral analysis, with application to the Gulf Stream. *Journal of Advances in Modeling Earth Systems*, e2021MS002692. doi: 10.1029/2021MS002692

Uchida, T., Rokem, A., Squire, D., Nicholas, T., Abernathey, R. P., Soler, S., ... others (2022). `xrft`*: Fourier transforms for xarray data.* Retrieved from `https://xrft.readthedocs.io/en/latest/` doi: 10.5281/zenodo.1402635

Vallis, G. (2006). *Atmospheric and Oceanic Fluid Dynamics.* Cambridge.

Yaglom, A. M. (2004). *An introduction to the theory of stationary random functions.* Mansfield Centre, CT: Martino Publishing.

Yang, Y., McWilliams, J. C., San Liang, X., Zhang, H., Weisberg, R. H., Liu, Y., & Menemenlis, D. (2021). Spatial and temporal characteristics of the submesoscale energetics in the Gulf of Mexico. *Journal of Physical Oceanography*, *51*(2), 475–489. doi: 10.1175/JPO-D-20-0247.1